

# Variable Parameter Admittance Control of Robot Based on a Virtual Force/Torque Sensor

Yanjiang Huang , Member, IEEE, Xinyu Liu , Jianhong Ke, Xianmin Zhang , Member, IEEE, Lixin Yang , and Jun Ota , Member, IEEE

**Abstract**—Admittance control enables supple control of a robot through force-motion mapping, allowing robots to actively adapt to forces exerted by humans during interaction, which are typically collected through force sensors. In addition, since the requirements for admittance control parameters vary at different stages of the task, it is necessary to propose a variable parameter strategy to improve task success rate and efficiency. Therefore, this article proposes a variable parameter admittance control without force sensors. First, The performance of the three observers in terms of estimation accuracy, computational efficiency, and parameter tuning is compared, and the virtual force/torque (F/T) sensor is designed accordingly. Second, a variable parameter admittance control with virtual F/T sensor is proposed to reduce the robot's recovery time after withdrawing the external force. The proposed method was verified on two robots with different degrees of freedom. The experimental results show that the estimated values of the virtual F/T sensor of both robots can follow the changes in the measured values. The variable parameter admittance control enables rapid response to external forces and improves work efficiency. Furthermore, the proposed method can complete the bearing assembly task.

**Index Terms**—Admittance control, disturbance observer, force/torque (F/T) sensor, robot dynamics.

## I. INTRODUCTION

RECENTLY, collaborative robots have become a popular direction in robotics research [1]. Human-robot interaction is one of the essential features of collaborative robots. Standard human-robot interaction methods, such as zero-force

Received 25 March 2025; revised 30 June 2025; accepted 27 July 2025. Recommended by Technical Editor N. Motoi and Senior Editor S. Katsura. This work was supported in part by the National Natural Science Foundation of China under Grant 52475016 and Grant U24A20108 and in part by the Guangzhou Municipal Scientific and Technological Project under Grant 2024A04J6287. (Corresponding author: Lixin Yang.)

Yanjiang Huang, Xinyu Liu, Jianhong Ke, Xianmin Zhang, and Lixin Yang are with the Guangdong Provincial Key Laboratory of Precision Equipment and Manufacturing Technology, South China University of Technology, Guangzhou 510640, China (e-mail: melxyang@scut.edu.cn).

Jun Ota is with the Research into Artifacts, Center for Engineering, The University of Tokyo, Tokyo 113-8656, Japan (e-mail: ota@race.t.u-tokyo.ac.jp).

Color versions of one or more figures in this article are available at <https://doi.org/10.1109/TMECH.2025.3595612>.

Digital Object Identifier 10.1109/TMECH.2025.3595612

control [2], drag-and-drop instruction [3], and admittance control [4] must be equipped with external F/T sensors to detect the force generated during human-robot interaction [5]. However, many newly developed lightweight robots are not equipped with built-in articulated torque sensors, such as the UR5 robot, due to the increased cost of the sensors, the load consumption, and the additional elasticity associated with torque sensors. Not only that, the data read from the force sensors may not be reliable under different operating conditions (temperature or humidity variations). Therefore, it is meaningful to conduct human-robot interaction experiments without external force/torque (F/T) sensors [6]. In this case, the design of disturbance observers based on the robot's dynamics model for detecting the magnitude of external forces can be used as an alternative to force sensors [7].

Disturbance observer in robotics rely on inverse dynamic models, where estimation accuracy directly depends on model precision [8]. Learning-based modeling approaches utilize neural networks to construct nonparametric models from experimental data [9]. While effective at capturing nonlinear dynamics, these models lack explicit physical parameter representations and often violate fundamental constraints, complicating their integration with observer designs requiring physical interpretability. In contrast, rigid-body dynamic identification focuses on deriving base parameters through physics-constrained modeling [10]. This approach ensures strict adherence to mechanical conservation laws, yielding explicit parameter formulations compatible with manipulator dynamics. The resulting model makes the observer inherently consistent with physical system constraints, thus providing more reliable real-world performance, which is critical for the deployment of safety-critical robotic systems.

Many studies have implemented the design of disturbance observers based on inverse dynamics models. A nonlinear observer is used to estimate the friction of a planar mechanical arm [11]. This method is computationally intensive and requires acceleration. However, acceleration is more likely to be overwhelmed by noise. Therefore, a generalized momentum-based observer has been proposed to eliminate the effect of acceleration, and this approach is extremely important for disturbance observers [12], [13]. However, it is sensitive to errors and disturbances in the joint actuators of the modeled robot. The collision detection threshold must be increased to prevent false alarms, which significantly reduces the detection sensitivity. To overcome this problem, low-pass or band-pass filters were introduced to separate the collision torque from the unmodularized dynamic effects

and measurement noise [14], [15]. Subsequently, there are based on extended state observers have been proposed, but the effectiveness of this approach depends on the order of the extended state [16]. Recently, Kalman filters have become widely used in observer applications [17] because the filter is a powerful tool for averaging out squared errors by minimizing them [18], [19]. The Kalman filter takes into account the model of the manipulator and the model of the disturbance, discarding the Jacobian and the inverse of inertia matrices [20], and effectively reduces the measurement and estimation noise. Therefore, the fusion application of disturbance observer and Kalman filter has been applied to motion control [21].

These observers have their advantages and disadvantages in terms of computational speed, memory consumption, degree of dependence on dynamical models, and difficulty of parameter adjustment. Therefore, it is necessary to have a unified scenario to make a comprehensive evaluation of various disturbances, including performance, computational efficiency, difficulty of parameter tuning, and other indicators [22].

One of the purposes of designing an observer, which allows the robot to sense external signal interference signals, is to enable control. Robots face changing environments during human interaction, so time-invariant admittance control is rigid in applications [23]. Numerous approaches have proposed variable parameter controllers to overcome the drawbacks of traditional methods [24], [25]. Estimating human motion intention based on human force and vertical object velocity in [26] and [27]. Cho et al. [28] proposed a damping adjustment scheme that takes into account external torque without sensors. Peng et al. [29] based on the interaction force and trajectory tracking consisting of the cost function to obtain the desired admittance parameters. The controller may be environmentally related, operator or task related [30]. In environment-related controllers, variable admittance control is used for contact with the environment rather than human intent [31]. Task-related controllers focus on specific tasks [32], such as obstacle avoidance or trajectory tracking. Moreover, many variable parameter strategies at this stage address the real-time intentions of the operators and are dedicated to conforming to human behavior [33]. However, when a robot is in a task scenario involving human-robot interaction, the guidance process requires the robot to be soft, while the recovery process requires the robot to be highly rigid. These two requirements are mutually contradictory. Therefore, We have set up the following scenario: When the robot motion is subjected to an external force, the robot deviates from its trajectory, and when the external force is withdrawn it should return to the reference trajectory as soon as possible to reduce the idle time of the robot to complete the preset task rapidly.

This article makes the following contributions to solve the above problems.

- 1) Derive a robot dynamics model and three disturbance observers based on our previous work [10]. By comparing the performance of these three observers in terms of estimation accuracy, computational efficiency, and parameter tuning, guidelines are given for selecting observers under different operating conditions. Design of a virtual F/T sensor for admittance control.

- 2) Adaptive admittance control based on virtual F/T sensor is proposed to achieve human-robot compliant, safe interaction, and reduced robot idle time. The proposed method has been verified the on 6-DoF UR5 and 7-DoF Franka Emika Panda robot and can complete assembly tasks.

The rest of this article is organized as follows. Section II derives robot dynamics model and models of three observers. Section III proposes the variable parameter controller based on the virtual F/T sensor. Section IV provides the experimental results on UR5 and Franka Emika Panda robot. Finally, Section V concludes this article.

## II. DISTURBANCE OBSERVER

### A. Robot Dynamics Model

In the absence of external forces, the dynamic model of an n-DoF series robot can be described as follows:

$$M(q)\ddot{q} + C(q, \dot{q})\dot{q} + G(q) + F_f = \tau_J \quad (1)$$

where  $q, \dot{q}, \ddot{q}, \tau_J$ , and  $F_f \in \mathbb{R}^n$  denote the joint angle, velocity, acceleration, driving torque, and friction torque, respectively,  $M(q) \in \mathbb{R}^{n \times n}$  is the positive definite and symmetric inertia matrix,  $C(q, \dot{q}) \in \mathbb{R}^{n \times n}$  is the centrifugal and Coriolis matrix,  $G(q) \in \mathbb{R}^n$  is the torque related to the gravity.

The left-hand side of (1) can be converted as follows:

$$\Phi_b(q, \dot{q}, \ddot{q})\beta_b = M(q)\ddot{q} + C(q, \dot{q})\dot{q} + G(q) + F_f \quad (2)$$

where  $\Phi_b(q, \dot{q}, \ddot{q}) \in \mathbb{R}^{n \times 14n}$  is known as the regression matrix. The  $\beta_b \in \mathbb{R}^{14n}$  is the base parameter vector. The specific computational procedure for the dynamic parameter identification can be found in our previous paper [10].

$\beta_b$  can be divided into two subsets, one subset consisting of inertia parameters related to the mass of the connecting rod and the inertia tensor matrix, denoted  $\beta_{ib}$ , and the other subgroup consisting of parameters related to the friction force, denoted  $\beta_f$ . Thus, (2) can be written as

$$\tau_J = \Phi_b(q, \dot{q}, \ddot{q})[\beta_{ib}^T \beta_f^T]^T. \quad (3)$$

The joint friction torque  $F_f$  can be written as

$$F_f = \Phi_b(q, \dot{q}, \ddot{q})[0 \ \beta_f^T]^T. \quad (4)$$

The torque associated with the inertia is written as

$$M(q)\ddot{q} + C(q, \dot{q})\dot{q} + G(q) = \Phi_b(q, \dot{q}, \ddot{q})[\beta_{ib}^T \mathbf{0}]^T. \quad (5)$$

For the convenience of subsequent numerical calculations, (5) is renamed

$$rneq(q, \dot{q}, \ddot{q}, g_0) = \Phi_b(q, \dot{q}, \ddot{q})[\beta_{ib}^T \mathbf{0}]^T \quad (6)$$

where  $g_0$  denotes the gravity acceleration vector. The identified dynamics model is coupled, i.e., the form on the left side of (6) is obtained instead of the form with the right terms separated. Therefore, an explicit expression for the terms on the right side of the equation cannot be obtained. It is possible to calculate the values of the right side of the equation for each set of joint data by means of numerical calculations.

For the inertia matrix  $M$ , let  $e_j = [0 \ \dots \ 1 \ \dots \ 0]^T$  denotes the n-dimensional unit vector with the element of the

$j$ th dimension being 1 and the other dimensions being 0. The  $j$ th  $M(:, j)$  column of the inertia matrix can be calculated by the following:

$$M(:, j) = rnea(q, \mathbf{0}, e_j, \mathbf{0}) \quad (7)$$

where  $\mathbf{0}$  denotes the zero vector. The numerical expression for the inertia matrix  $M(q)$  is obtained by combining all  $M(:, j)$  obtained.

Define the generalized momentum of a robotic system as:

$$p = M\dot{q} = rnea(q, \mathbf{0}, \dot{q}, \mathbf{0}). \quad (8)$$

Compute the variable  $\dot{M}\dot{q}$

$$\dot{M}\dot{q} = \sum_{i=1}^n \frac{(\partial M)}{\partial q_i} \dot{q}_i. \quad (9)$$

Numerical differentiation of (9)

$$\dot{M}\dot{q} \approx \sum_{i=1}^n \frac{(M(q + \Delta q_i) - M(q))\dot{q}}{\Delta q} \dot{q}_i \quad (10)$$

where  $\Delta q$  denotes the joint angle increment. In this article,  $\Delta q = 10^{-7}$ .  $\Delta q_i$  is an auxiliary vector, the first  $i$  element is  $\Delta q$ , and the remaining elements are zero.

Substituting the (8) into (10), the equation is

$$\dot{M}\dot{q} \approx \sum_{i=1}^n \frac{rnea(q + \Delta q_i, \mathbf{0}, \dot{q}, \mathbf{0}) - rnea(q, \mathbf{0}, \dot{q}, \mathbf{0})}{\Delta q} \dot{q}_i. \quad (11)$$

$C\dot{q}$  can be numerically computed by the following:

$$C\dot{q} = rnea(q, \dot{q}, \mathbf{0}, \mathbf{0}). \quad (12)$$

Since  $\dot{M} - 2C$  is an antisymmetric matrix, and  $\dot{M}$  is a symmetric matrix that can be obtained [34]

$$\dot{M} = C + C^T. \quad (13)$$

The variable  $C^T\dot{q}$  is

$$C^T\dot{q} = \dot{M}\dot{q} - C\dot{q}. \quad (14)$$

Substituting (11 and 12) into (14):

$$C^T\dot{q} \approx \sum_{i=1}^n \frac{rnea(q + \Delta q_i, \mathbf{0}, \dot{q}, \mathbf{0}) - rnea(q, \mathbf{0}, \dot{q}, \mathbf{0})}{\Delta q} \dot{q}_i - rnea(q, \dot{q}, \mathbf{0}, \mathbf{0}). \quad (15)$$

$G(q)$  can be calculated by the following:

$$G(q) = rnea(q, \mathbf{0}, \mathbf{0}, g_0). \quad (16)$$

When the robot is subjected to an external force,  $\tau_J$  is divided into two parts:  $\tau$ , the known joint drive torque generated by the controller, and  $\tau_{ext}$ , the unknown joint torque due to external contact forces

$$\tau_J = \tau_{ext} + \tau. \quad (17)$$

The dynamics of the series robot (1) should be modified

$$M(q)\ddot{q} + C(q, \dot{q})\dot{q} + G(q) + F_f = \tau_{ext} + \tau. \quad (18)$$

However,  $\ddot{q}$  introduces a lot of noise that drowns out the  $\tau_{ext}$ . Therefore, the design goals of the observer is to accurately estimate the  $\tau_{ext}$  without using the  $\ddot{q}$ .

## B. Filtered Dynamics Disturbance Observer (FDO)

In order to eliminate the  $\ddot{q}$  in (18), it is necessary to select a filter  $f_1(t) = \mathcal{L}^{-1}(F_1(s)) = \omega e^{-\omega t}$  whose Laplace transform is

$$F_1(s) = \frac{\omega}{s + \omega} \quad (19)$$

where  $s$  is multiparameter variable [35]. The observer is described as

$$f_1(t) * \tau_{ext} = f_1(t) * \{M\ddot{q} + C\dot{q} + F_f + G - \tau\} \quad (20)$$

where  $*$  represents the convolution operation. Equation (20) can be rewritten as

$$f_1(t) * \tau_{ext} = f_1(t) * \{C\dot{q} + F_f + G - \tau - \dot{M}\dot{q}\} + f_1(t) * \{M\ddot{q} + \dot{M}\dot{q}\}. \quad (21)$$

Substituting (14) into (21), then the first term to the right of (21) can be simplified as

$$f_1(t) * \{C\dot{q} + F_f + G - \tau - \dot{M}\dot{q}\} = f_1(t) * \{-\mu\} \quad (22)$$

where  $\mu = C^T\dot{q} - G - F_f + \tau$ , the terms are obtained from (4), (15), and (16), respectively. The second term to the right of (21) can be calculated as

$$f_1(t) * \{M\ddot{q} + \dot{M}\dot{q}\} = \int_0^t (f_1(t-r)(M\ddot{q} + \dot{M}\dot{q}))dr \quad (23)$$

which can simplified as follows:

$$f_1(t) * \{M\ddot{q} + \dot{M}\dot{q}\} = f_1(0)M\dot{q} - f_1(t)M_0\dot{q}_0 + \dot{f}_1(t) * \{M\dot{q}\}. \quad (24)$$

Define a new filter  $f_2(t) = \dot{f}_1(t) = -\omega^2 e^{-\omega t}$ , whose Laplace transform is

$$F_2(s) = -\frac{\omega^2}{s + \omega}. \quad (25)$$

Finally, the observer can be described as follows:

$$f_1(t) * \tau_{ext} = f_1(t) * \{-\mu\} + f_2(t) * p + \omega p. \quad (26)$$

The left side of (26) can be viewed as a low-pass filtering of the external force-induced joint external force  $\tau_{ext}$ . All constituent terms on the right-hand side of (26) can be derived from (4), (16), (15), and (8) without the  $\ddot{q}$ .

According to the bilinear transformation, the filters  $F_1(s)$  and  $F_2(s)$  can be transformed as, respectively

$$H_1(z) = \frac{z + 1}{\left(\frac{2f_s}{\omega} + 1\right)z + \left(1 - \frac{2f_s}{\omega}\right)} \quad (27)$$

$$H_2(z) = \frac{-\omega(z + 1)}{\left(\frac{2f_s}{\omega} + 1\right)z + \left(1 - \frac{2f_s}{\omega}\right)} \quad (28)$$

where  $s = 2f_s \frac{z-1}{z+1}$  and  $f_s$  is sampling frequency. Combining (27) and (28), and based on the inverse bilinear transformation, the discretized form of (26) is, then

$$\begin{aligned} \hat{\tau}_{ext} = & k_1 (\mathbf{Y}_1^{t-1} + \mathbf{Y}_2^{t-1}) - k_2 (\boldsymbol{\mu}^t + \boldsymbol{\mu}^{t-1}) \\ & + k_3 (\mathbf{p}^t + \mathbf{p}^{t-1}) + \omega \mathbf{p}^t \end{aligned} \quad (29)$$

where  $\hat{\tau}_{ext}$  is the estimated value of the  $\tau_{ext}$ ,  $\mathbf{Y}_1$  is the value of  $-\boldsymbol{\mu}$  filtered by (27),  $\mathbf{Y}_2$  is the value of  $\mathbf{p}$  filtered by (28), and  $(*)^t$  denotes the value of  $(*)$  at moment  $t$ ,  $k_1 = \frac{1-\frac{\omega}{2f_s}}{1+\frac{\omega}{2f_s}}$ ,  $k_2 = \frac{\frac{\omega}{2f_s}}{1+\frac{\omega}{2f_s}}$ , and  $k_3 = \frac{-\frac{\omega}{2f_s}}{1+\frac{\omega}{2f_s}}$ .  $f_s = 1/T_s$  is the sampling frequency.

The computational complexity is:  $\mathcal{O}(n)$ . The cutoff frequency  $\omega$  is the only function that needs to be adjusted.  $\omega$  should be greater than the frequency of the measured torque. The FDO relies on a low-pass filter design with a cutoff frequency  $\omega$  that satisfies  $\omega \gg f_s$ . If  $f_s$  decreases,  $\omega$  needs to be reduced, otherwise the signal will be aliased, and the high-frequency torque cannot be detected.

### C. Generalized Momentum Observer (GMO)

The design principle of GMO is as follows:

$$\hat{\tau}_{ext} = \mathbf{K}(\mathbf{p} - \hat{\mathbf{p}}) \quad (30)$$

where the superscript  $\hat{\cdot}$  represents the observed value of  $(\cdot)$ , and  $\mathbf{K}$  is the gain matrix, which is generally diagonal. The GMO is designed by calculating the difference between the generalized momentum and the observed generalized momentum [36]. The differentiation of (30) is

$$\dot{\hat{\tau}}_{ext} = \mathbf{K}(\dot{\mathbf{p}} - \dot{\hat{\mathbf{p}}}). \quad (31)$$

The time differential of the generalized momentum  $\dot{\mathbf{p}}$  is obtained from (8) as

$$\dot{\mathbf{p}} = \dot{\mathbf{M}}\dot{\mathbf{q}} + \mathbf{M}\ddot{\mathbf{q}}. \quad (32)$$

Combining (32), (18), and (14),  $\dot{\mathbf{p}}$  and  $\dot{\hat{\mathbf{p}}}$  can be calculated as follows:

$$\dot{\mathbf{p}} = \boldsymbol{\mu} + \tau_{ext}, \dot{\hat{\mathbf{p}}} = \boldsymbol{\mu} + \hat{\tau}_{ext}. \quad (33)$$

Substituted (33) into (31) and integrated to obtain the final expression

$$\hat{\tau}_{ext} = \mathbf{K} \left\{ \mathbf{p} - \mathbf{p}_0 - \int_0^t (\boldsymbol{\mu} + \hat{\tau}_{ext}) dt \right\} \quad (34)$$

where  $\mathbf{p}_0$  is the initial generalized momentum. Discretize (34) using the trapezoidal formula

$$\hat{\tau}_{ext} = \mathbf{K} \left\{ \mathbf{p}^t - \mathbf{p}^0 - \sum_{i=0}^t \left( \frac{\mathbf{u}^i + \hat{\tau}_{ext}^{i-1} + \mathbf{u}^{i-1} + \hat{\tau}_{ext}^{i-2}}{2f_s} \right) \right\}. \quad (35)$$

The computational complexity is:  $\mathcal{O}(n)$ . Equation (35) is discretized based on the trapezoidal integration formula and is sensitive to the integration step size  $T_s$ . A larger  $T_s$  increases the cumulative error of the observer and leads to phase delays. smaller  $T_s$  results in oscillations in the observer.

### D. Kalman Filter Disturbance Observer (KFO)

The external force is modeled as

$$\dot{\tau}_{ext} = \mathbf{A}_\tau \tau_{ext} + \mathbf{w}_\tau \quad (36)$$

where  $\mathbf{A}_\tau \in \mathbb{R}^{n \times n}$  describes the change trend of external force  $\tau_{ext}$ . When external forces cannot be accurately modeled,  $\mathbf{A}_\tau = \mathbf{0}$ .  $\mathbf{w}_\tau \in \mathbb{R}^n$  is the external force error vector, which follows the Gaussian distribution  $\mathbf{w}_\tau \sim \mathcal{N}(\mathbf{0}, \mathbf{Q}_\tau)$ , and  $\mathbf{Q}_\tau$  is the covariance matrix of the external force error.

Equation (33) is rewritten as

$$\dot{\mathbf{p}} = \boldsymbol{\mu} + \tau_{ext} + \mathbf{w}_p \quad (37)$$

$\mathbf{w}_p \in \mathbb{R}^n$  is the error generated in the process of robot dynamics modeling, mainly caused by inaccurate joint friction modeling and satisfies the Gaussian distribution  $\mathbf{w}_p \sim \mathcal{N}(\mathbf{0}, \mathbf{Q}_p)$  and  $\mathbf{Q}_p$  are the covariance matrix, respectively [20].

Letting state vector  $\mathbf{x} = [\mathbf{p}^T, \tau_{ext}^T]^T$ , (36) and (37) are united as

$$\begin{cases} \dot{\mathbf{x}} = \mathbf{A}_c \mathbf{x} + \mathbf{B}_c \boldsymbol{\mu} + \mathbf{w} \\ \mathbf{y} = \mathbf{C}_c \mathbf{x} + \mathbf{v} \end{cases} \quad (38)$$

where the matrix of coefficients is

$$\mathbf{A}_c = \begin{bmatrix} \mathbf{0} & \mathbf{I} \\ \mathbf{0} & \mathbf{A}_\tau \end{bmatrix}, \quad \mathbf{B}_c = \begin{bmatrix} \mathbf{I} \\ \mathbf{0} \end{bmatrix}, \quad \mathbf{C}_c = [\mathbf{I} \quad \mathbf{0}] \quad (39)$$

where  $\mathbf{I}$  is identity matrix.  $\mathbf{w}$  is the process noise, which satisfy the Gaussian distribution  $\mathbf{w} \sim \mathcal{N}(\mathbf{0}, \mathbf{Q})$  and its corresponding covariance matrix is:  $\mathbf{Q} = \text{diag}\{\mathbf{Q}_p, \mathbf{Q}_\tau\}$ .  $\mathbf{v} \in \mathbb{R}^n$  is the noise vector, which satisfies the Gaussian distribution  $\mathbf{v} \sim \mathcal{N}(\mathbf{0}, \mathbf{R}_c)$ .  $\mathbf{R}_c$  is the covariance matrix corresponding to the measurement noise.

Equation (38) describes the state space model of a continuous system, and it needs to be discretized as

$$\begin{cases} \mathbf{x}^t = \mathbf{A}_c^t \mathbf{x}^{t-1} + \mathbf{B}_c^t \boldsymbol{\mu}^t + \mathbf{w}^t \\ \mathbf{y}^t = \mathbf{C}_c^t \mathbf{x}^t + \mathbf{v}^t \end{cases} \quad (40)$$

where  $\mathbf{w}^t \sim \mathcal{N}(\mathbf{0}, \mathbf{Q}^t)$  and  $\mathbf{v}^t \sim \mathcal{N}(\mathbf{0}, \mathbf{R}_c^t)$ . Common discretization methods include forward Euler (FE) and zero order hold (ZOH) [37]. The FE method is simple to implement, and the ZOH method is more accurate.

The FE method is

$$\mathbf{A}_c^t = \mathbf{I} + T_s \mathbf{A}_c, \quad \mathbf{B}_c^t = T_s \mathbf{B}_c, \quad \mathbf{C}_c^t = \mathbf{C}_c \quad (41)$$

where  $T_s$  is the sampling time matrix. Process noise and measurement noise, respectively

$$\mathbf{Q}^t = T_s^2 \mathbf{Q}, \mathbf{R}_c^t = \mathbf{R}_c / T_s. \quad (42)$$

The computational complexity is:  $\mathcal{O}(n^2)$ .

In the ZOH method,  $\mathbf{A}^t$  and  $\mathbf{B}^t$  satisfy the following:

$$\begin{bmatrix} \mathbf{A}^t & \mathbf{B}^t \\ \mathbf{0} & \mathbf{I} \end{bmatrix} = \exp \left( \begin{bmatrix} \mathbf{A}_c & \mathbf{B}_c \\ \mathbf{0} & \mathbf{0} \end{bmatrix} T_s \right) \quad (43)$$



where  $\exp()$  represents the exponential matrix. The process noise  $Q^t$  is calculated as follows:

$$\begin{bmatrix} M_{11}^t & M_{12}^t \\ \mathbf{0} & M_{22}^t \end{bmatrix} = \exp \left( \begin{bmatrix} A_c & Q_c \\ \mathbf{0} & -A_c \end{bmatrix} T_s \right) \\ Q^t = M_{12}^t (M_{11}^t)^T \quad (44)$$

where  $M_{11}^t$ ,  $M_{22}^t$ , and  $M_{12}^t$  are adjunct matrix, while the output matrix  $C^t$  and the measurement covariance matrix  $R_c^t$  are calculated in the same form. The computational complexity is:  $O(n^3)$ .

With the discretized state space, the external torque can be obtained iteratively through the Kalman filter [20].

As can be seen from (41), the FE method has higher approximation accuracy, when  $T_s$  is small, but it introduces state prediction error as  $T_s$  increases. The observer effect depends more and more on the process noise (as can be seen from (42)). In this article, the exponential matrix in the ZOH is approximated using a fifth-order Taylor expansion. The ZOH degenerates to FE when the approximation is performed using a first-order Taylor expansion. The integration error of the ZOH grows with increasing  $T_s$  but remains more robust than that of the FE. This is because the truncation error of the FE leads to state prediction bias, whereas the ZOH maintains stability through higher order Taylor expansion.

### III. VARIABLE PARAMETER ADMITTANCE CONTROL BASED ON VIRTUAL F/T SENSOR

The model of Cartesian space admittance control is

$$M_d \ddot{\tilde{X}} + B_d \dot{\tilde{X}} + K_d \tilde{X} = F_{ext} \quad (45)$$

where  $\tilde{X}$  is the pose deviation of the center of the end flange of the robot in Cartesian space, defined as  $\tilde{X} = X - X_d$ . Here,  $X$  and  $X_d$  is the robot's actual pose and the target pose.  $M_d, B_d, K_d \in \mathbb{R}^{n \times n}$  are the expected inertia matrix, damping matrix, and stiffness matrix, respectively, and are generally set as diagonal matrices. Only the controller at the initial position and orientation is considered, that is,  $\ddot{\tilde{X}}_d = \dot{\tilde{X}}_d = 0$ .  $F_{ext} \in \mathbb{R}^n$  is the external force applied to the Cartesian space at the end of the robot, which can be calculated by the observer constructed in the Section II. The mapping relationship between the two is:

$$F_{ext} = (J_F^T)^{-1} \tau_{ext} \quad (46)$$

where  $J_F^T$  is the transpose of the robot's Jacobian matrix  $J_F$ .

In order to reduce the motion time of the robot in the recovery phase after removing the external force, a variable parameter controller is proposed in this article. Let the stiffness matrix  $K_d$  and inertia matrix  $M_d$  be modulated by velocity  $\dot{\tilde{X}}$ . The diagonal elements of stiffness matrix  $K_{dva}$ , inertia matrix  $M_{dva}$ , and damping matrix  $B_{dva-i}$  in the phase of removing external forces are calculated as follows:

$$K_{dva-i} = \alpha K_{di} e^{|\dot{\tilde{X}}_i|} \\ M_{dva-i} = \frac{M_{di} e^{-|\dot{\tilde{X}}_i|}}{\alpha}$$

$$B_{dva-i} = 2\xi \sqrt{M_{dva-i} K_{dva-i}} \quad (47)$$

where  $\alpha$  is a constant.

The larger  $M_{dva}$  is, the larger the inertia is, and the better the smoothness of motion is. If  $M_{dva}$  is too small, it will lead to a too large position increment and make the robot out of the Cartesian space. The larger  $K_{dva}$  is, the greater the stiffness and the higher the precision of position control. It is worth mentioning that when  $K_{dva}$  is zero, the admittance control degrades to drag oscillography. The damping matrix  $B_{dva}$  is adjusted according to the damping ratio  $\xi$ . A large force is required to drag the robot if the damping ratio is too large. If the  $\xi$  is too small, the robot will oscillate reciprocally around the initial position. When external force are removed, the stiffness matrix  $K_{d-i}$  will suddenly increase, and the inertia matrix  $M_{d-i}$  will suddenly decrease. As the robot returns to the target pose  $X_d$ , velocity  $\dot{\tilde{X}}$  approaches 0, and the stiffness matrix and inertia matrix will return to the initial set values.

The robot's motion state can be divided into two phases: the robot moves under an external force, and after the force is removed, it returns to its initial position. In combination with (47), the control strategy (45) is rewritten as

$$M_{dva} \ddot{\tilde{X}} + B_{dva} \dot{\tilde{X}} + K_{dva} \tilde{X} = F_{ext}. \quad (48)$$

Acceleration, velocity and position are as follows:

$$\ddot{\tilde{X}}^t = M_{dva}^{-1} (F_{ext} - B_{dva} \dot{\tilde{X}}^{t-1} - K_{dva} \tilde{X}^{t-1}) \quad (49)$$

$$\dot{\tilde{X}}^t = \dot{\tilde{X}}^{t-1} + \ddot{\tilde{X}}^t T_s \quad (50)$$

$$X^t = X^{t-1} + \dot{\tilde{X}}^t T_s. \quad (51)$$

To achieve large acceleration, combining (47) and (49),  $\alpha$  should be greater than zero, and the larger the better.

Design the following Lyapunov function:

$$V = \frac{1}{2} \dot{\tilde{X}}^T M_{dva} \dot{\tilde{X}} + \frac{1}{2} \tilde{X}^T K_{dva} \tilde{X}. \quad (52)$$

$M_{dva}$  and  $K_{dva}$  are positive definite matrices, so  $V > 0$  when  $\dot{\tilde{X}} \neq 0$  or  $\tilde{X} \neq X_d$ , and  $V = 0$  when  $\dot{\tilde{X}} = \tilde{X} = 0$ . The derivative of  $V$  is

$$\dot{V} = \dot{\tilde{X}}^T M_{dva} \ddot{\tilde{X}} + \tilde{X}^T K_{dva} \dot{\tilde{X}}. \quad (53)$$

Equation (49) is substituted into (53) with

$$\dot{V} = \dot{\tilde{X}}^T (F_{ext} - B_{dva} \dot{\tilde{X}} - K_{dva} \tilde{X}) + \tilde{X}^T K_{dva} \dot{\tilde{X}} \quad (54)$$

$$= \dot{\tilde{X}}^T F_{ext} - \dot{\tilde{X}}^T B_{dva} \dot{\tilde{X}}. \quad (55)$$

Since  $K_{dva}$  is a symmetric matrix, (54) can be transformed to (55). This variable parameter strategy works after the withdrawal of the external force ( $F_{ext} = \mathbf{0}$ ), when  $\dot{V} \leq 0$ ,  $\dot{V} = 0$  only when  $\dot{\tilde{X}} = \mathbf{0}$ . According to Lashalle's invariant set principle, the proposed control strategy converges asymptotically to the desired position  $X_d$ . The computational complexity of admittance control is  $O(n)$ , so the computational complexity of variable parameter admittance control based on virtual F/T sensor is  $O(n^2)$ .

---

**Algorithm 1:** Algorithm of Variable Parameter Admittance Control Based on Virtual F/T Sensor.

---

```

1: Input: Joint position  $q^0$ , speed  $\dot{q}^0$ , torque  $\tau^0$ 
2: repeat
3:   Virtual F/T sensor detects external forces:  $F_{ext}$ 
4:   if  $F_{ext} > F_{tsd}$  then
5:     Reset the parameter matrix  $M_d, B_d, K_d$ .
6:   else
7:     Update the parameter matrix: (47).
8:   end if
9:   Update the Cartesian acceleration  $\ddot{X}^t$ : (49)
10:  Update the Cartesian speed  $\dot{X}^t$ : (50)
11:  if  $\dot{X}^t > \dot{X}_{tsd}^t$  then
12:     $\dot{X}^t = \dot{X}_{tsd}^t$ 
13:  end if
14:  Update Cartesian position deviation: (51)
15:  Inverse kinematics to solve joint space angle:  $q^t$ 
16:  Robot position control
17: until Back to initial position

```

---

In order to ensure safety, speed thresholds ( $\dot{X}_{tsd}$ ) need to be set to prevent dangers associated with robots moving too fast. The control process is shown in Algorithm 1.

#### IV. EXPERIMENTS

This article verifies the proposed method on a 6-DoF UR5 and a 7-DoF Franka Emika Panda robot.

##### A. Joint Space External Force Detection for UR5

The sampling frequency  $f_s$  is 125 Hz. The discrete interval  $T_s$  required for both observers and admittance control is 8 ms. Processor model is Intel (R) Core (TM) i7-6500U CPU @2.50 GHz 2.60 GHz. Use a interface (RTDE) to implement control and get data from UR5 robot. UR5 does not have torque sensors and the drive torque can only be obtained by means of electric current:  $\tau = K_i \dot{i}_m$ , where  $K_i = (12.625, 12.1625, 12.625, 9.3122, 9.3122, 9.3122)$ . The dashed box section in Fig. 1 shows this.

We design the experiment to verify the estimation performance of observers for  $\tau_{ext}$ . The end of the robot is allowed to perform repetitive circular motion on the horizontal plane with a radius of 0.2 m, a trajectory period of 4 s, and a running cycle of 5 cycles. In the first cycle, the robot moved freely, as shown in Fig. 2(a). Starting from the second cycle, the experimenter applies an external force to the robot, as shown in Fig. 2(b). The difference in current between the two cycles is considered as the true value of the external force [38]. The robot runs on essentially the same trajectory (orientation and velocity) in both cycles, so the reducer friction has the same orientation and magnitude. By subtracting the currents of the two cycles, the reducer friction will also cancel each other out. Obtaining joint torque from joint currents is a common indirect measurement method [39], but this really does not take into account factors, such as reducer friction, which will be a future direction of work.

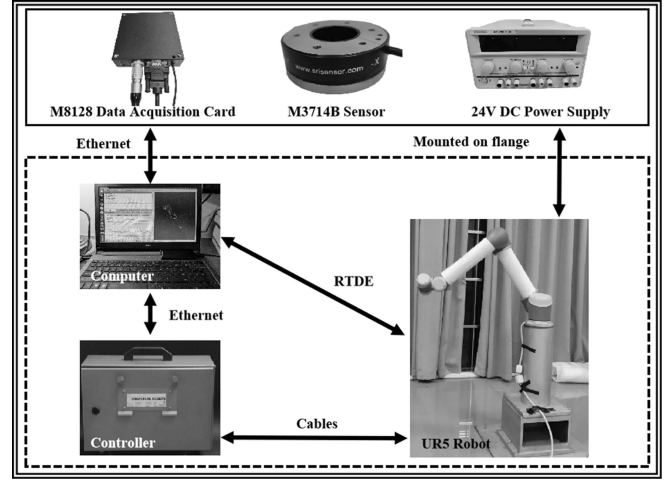


Fig. 1. Experimental equipment for UR5.

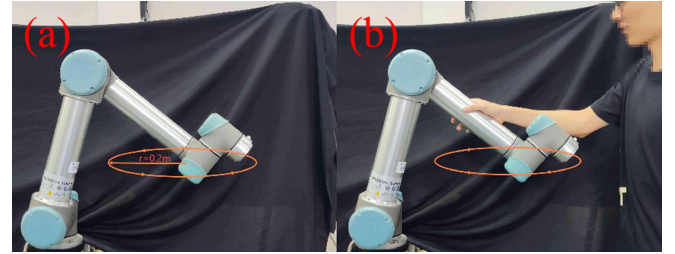


Fig. 2. Diagram of applied force. (a) First period: free movement. (b) Second period: struck by an external force.

The parameters of each observer are as follows.

- 1) FDO:  $\omega = 10$
- 2) GMO:  $K = \text{diag}(5, 3, 4, 10, 10, 10)$
- 3) FKO:  $R = \text{diag}(0.5, 0.5, 0.5, 1.3, 1.3, 1.3)$   
 $Q_p = \text{diag}(0.01, 0.01, 0.01, 0.02, 0.02, 0.02)$   
 $Q_\tau = \text{diag}(5000, 5000, 5000, 5000, 5000, 5000)$ .

In Fig. 3, the black solid line is the  $\tau_{ext}$  obtained from the current difference. No external force was applied to the UR5 robot during the first cycle, but the estimated external force fluctuated around zero, indicating that there was an error in the external force output observed. From the second period onwards, all three observers tracked the changes in the external force well. For joint 2, the FDO estimate has the largest deviation because the parameter  $\omega$  must be selected for all joints. For joint 3, the hysteresis of FDO and GMO is more pronounced than that of KFO.

As in Table I, for joints 1, 2, and 3, KFO has the smallest root mean square error (RMSE). For joints 4 and 5, GMO has the smallest RMSE, but performs similarly to the other observers. For joint 6, all observers perform similarly; KFO performs best at the first three joints, but GMO performs slightly better at the last three joints. Overall, KFO has the best performance.

The robot's end runs different trajectories, and a total of 30 060 sets of joint data were collected. As seen from Table II, the average computation time per observation for the KFO (ZOH) is 5.7 times that of the FDO and GMO and 3.3 times that of

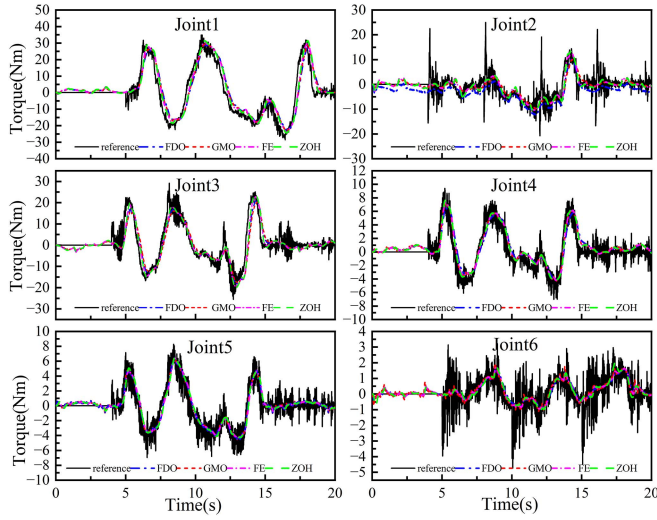


Fig. 3. Estimation of real time-varying external forces by observers.

TABLE I  
RMSE OF THREE OBSERVERS

Joint	FDO (Nm)	GMO (Nm)	FE (Nm)	ZOH (Nm)
1	5.6601	5.2106	4.7472	4.8555
2	4.2443	3.8767	3.6219	3.6475
3	4.6620	5.1080	4.0874	4.1538
4	1.5379	1.2939	1.3828	1.3345
5	1.2137	1.1976	1.3221	1.3164
6	0.9443	0.9322	0.9355	0.9440

TABLE II  
COMBINED PERFORMANCE OF THE THREE OBSERVERS

Method	Total sample	Computation time (s)	Average computation time (ms)	Difficulty of references
FDO	30 060	10.8690	0.3615	easy
GMO	30 060	10.5406	0.3506	hard
FE	30 060	17.5776	0.5847	difficult
ZOH	30 060	58.3627	1.9415	difficult

the FE discretization. This is because the fifth-order Taylor expansion of the exponential matrix in the computation of the ZOH discretization requires the calculation of the fifth power of the matrix [40].

The adjustment difficulty is evaluated. For a 6-DoF robot, FDO only needs to adjust the  $\omega$ . The GMO needs to adjust  $K$ , which contains six elements, so the adjustment is not difficult. The KFO needs to adjust  $Q$  and  $R_e$ , which contain 18 parameters, and the adjustment process is complicated.

We propose several guidelines for the selection of observers

- 1) GMO and FDO with high computational efficiency and low response time should be selected for collision detection. Because collisions often occur in a split second, which requires a fast response from the observer.
- 2) FDO has a frequency selection function that enables safe response. FDO filters out the high-frequency noise

and retains the low-frequency forces occurring from the human action to enable the robot to make an avoidance.

- 3) The KFO with high estimation accuracy should be selected for external force estimation. The FKO discretized by the ZOH has the highest accuracy, while the FE discretization has good computational efficiency.

## B. Cartesian Space External Force Detection for UR5

The KFO discretized by FE with better precision and shorter calculation time is chosen for the design. The M3714B sensor is mounted on the flange at the end of the robot and is used to compare with the virtual F/T sensor to verify validity. The M3714B sensor has been calibrated at the factory, so after mounting it to the robot flange, set its reading to zero. The zero drift of the sensor reading was ( $F_x$ ,  $F_y$ ,  $F_z$ ,  $T_x$ ,  $T_y$ , and  $T_z$ ): ( $-0.005984$ ,  $-0.086935$ ,  $0.024707$ ,  $-0.001477$ ,  $0.000072$ , and  $-0.000161$ ). The force applied to the sensor is captured by the M8128 data acquisition card, which filters the F/T signal, as shown in the double solid line portion of Fig. 1.

The frame of the end flange (denoted as frame F) is used as the reference frame for the sensor. The F/T sensor frame is noted as frame S. The transformation from frame S to frame F is related as follows:

$$\begin{bmatrix} \mathbf{F}_F^{\text{sen}} \\ \mathbf{N}_F^{\text{sen}} \end{bmatrix} = \begin{bmatrix} \mathbf{R}_F^S & \mathbf{0} \\ \mathbf{P}_F^S \mathbf{R}_S^F & \mathbf{R}_F^S \end{bmatrix} \begin{bmatrix} \mathbf{F}_S^{\text{sen}} \\ \mathbf{N}_S^{\text{sen}} \end{bmatrix} \quad (56)$$

$$\mathbf{P}_F^S = \begin{bmatrix} 0 & -p_z & p_y \\ p_z & 0 & -p_x \\ -p_y & p_x & 0 \end{bmatrix} \quad (57)$$

where  $\mathbf{F}_S^{\text{sen}}$  and  $\mathbf{N}_S^{\text{sen}} \in \mathbb{R}^3$  denote the vector representation of the force and torque readings of the sensor under the frame S, respectively.  $\mathbf{F}_F^{\text{sen}}$  and  $\mathbf{N}_F^{\text{sen}} \in \mathbb{R}^3$  denote the representations of the force and torque readings of the transducer under the frame F, respectively.  $\mathbf{R}_F^S \in \mathbb{R}^{6 \times 6}$  denotes the rotation matrix transformed from the sensor frame S to the frame F.  $\mathbf{P}_F^S$  denotes the antisymmetric matrix operator. Equation (46) is rewritten as  $[(\mathbf{F}_F^{\text{vir}})^T (\mathbf{N}_F^{\text{vir}})^T]^T = (\mathbf{J}_F^T)^{-1} \boldsymbol{\tau}_{\text{ext}}$ .

In this experiment, only external force can be applied to the sensor mounted on the robot flange. Install a 3-D-printed handle (of negligible weight) on the other side of the sensor so that the experimenter can drag the robot.

In Fig. 4, virtual F/T sensor can sensitively detect external force. When no external force is applied, the output of the virtual F/T sensor is not zero.  $F_x$ ,  $F_z$ ,  $T_y$ , and  $T_z$  can accurately track the external force.  $F_y$  and  $T_x$  are present to produce a bias. This may be due to virtual sensor accuracy or force sensor self-weight. Therefore, the sensor can be calibrated by considering them as loads to reduce the effect of their self-weight [41]. The RMSE of force and torque is less than 6 N and 0.65 Nm, respectively, and the errors are within a reasonable range. So, the proposed virtual F/T sensor can be used as a substitute for the real F/T sensor.

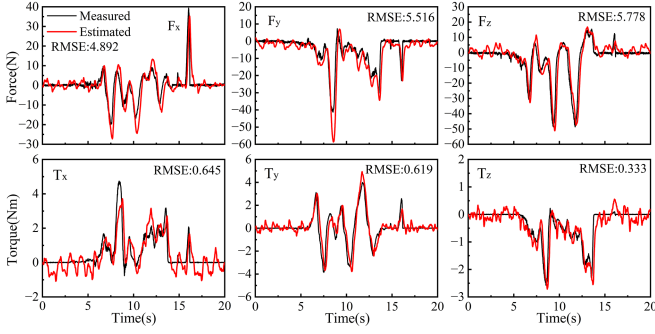


Fig. 4. Real sensor versus virtual sensor for UR5.

TABLE III  
PARAMETERS OF ADMITTANCE CONTROL FOR UR5

Coordinates	$M_d$	$B_d$	$K_d$	$\alpha$	$F_{tsd}$	$\dot{X}_{tsd}$
x	3	5	8	1.6	20 N	0.9 m/s
y	3	5	8	1.6	20 N	0.9 m/s
z	3	5	8	1.6	20 N	0.9 m/s
rx	0.1	0.3	0.5	1.6	6 Nm	-
ry	0.1	0.3	0.5	1.6	6 Nm	-
rz	0.1	0.3	0.5	1.6	6 Nm	-



Fig. 5. Cartesian spatial position admittance control.

### C. Variable Parameter Admittance Control Based on Virtual F/T Sensor for UR5

This experiment is divided into position control and orientation control in Cartesian space. The parameter settings related to the Cartesian spatial controller are finally shown in Table III.

1) *Cartesian Spatial Position Admittance Control*: At first, the UR5 robot is at its initial position. Then, the experimenter starts dragging the robot end handle to apply an external force, as shown in Fig. 5. If the external force exceeds  $F_{tsd}$ , the robot begins to move according to the controller (48). The larger the applied force, the faster the robot moves, but the maximum speed is less than  $\dot{x}_{tsd}$ . When the experimenter releases the handle, the robot will return to its initial position. Throughout the process, the position of the robot flange centre changes, but the direction remains the same.

Fig. 6(a) contains two stages of external force action. The displacement of the UR5 robot is shown in Fig. 6(b). During force application phases, the virtual F/T sensor exhibited a 0.24 s latency from force detection (6.52 s) to positional adjustment (6.76 s) in Phase I, and an equivalent 0.28 s delay from detection (17.72 s) to positional response (18.00 s) in Phase II. For force withdrawal scenarios, the system showed 0.26 s (8.60 s  $\rightarrow$  8.86 s) and 0.12 s (20.16 s  $\rightarrow$  20.28 s) recovery latencies in respective

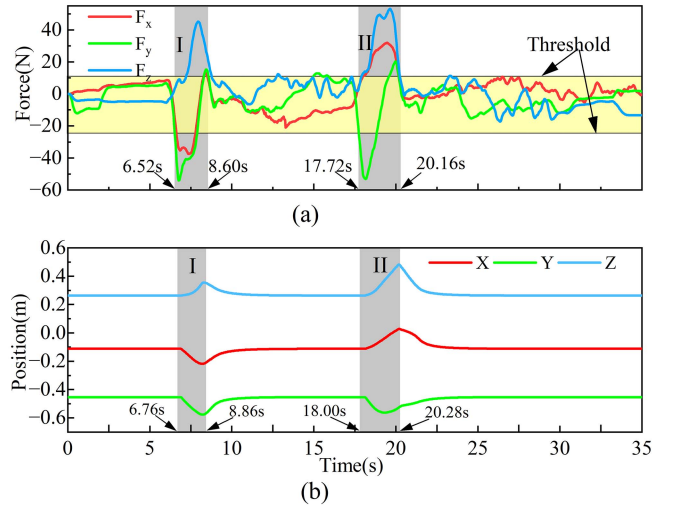
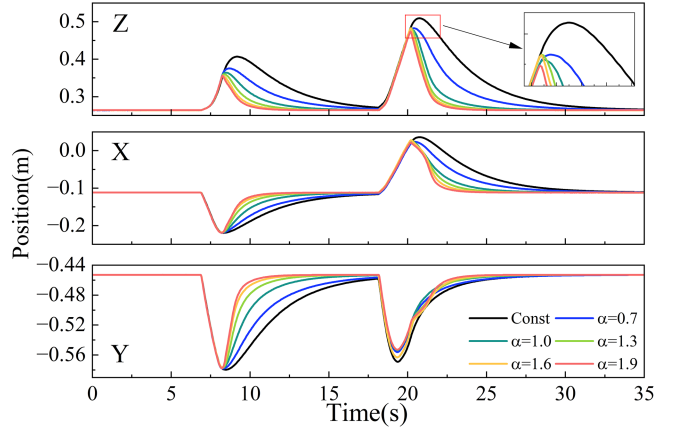


Fig. 6. Cartesian space position admittance control experiment. (a) Force estimates for virtual F/T sensor. (b) Position of the flange center in the base frame. The gray area represents the external force received by the robot during this period, and the yellow area indicates the set threshold range.

Fig. 7. Comparative experiment of Cartesian space position admittance.  $M_d$ ,  $B_d$ , and  $K_d$  were the same as in previous experiments. In order to maintain a single variable, the forces for this series of experiments were those recorded in Fig. 6 and not applied by the experimenter.

phases. The maximum observed latency between force detection and robotic response remained below 0.3 s throughout all trials.

As in Fig. 7, the proposed variable-parameter admittance control can bring the robot back to the initial position faster than the traditional method. The reason for this is that when the experimenter withdraws the external force, the stiffness  $K_{dva}$  will suddenly increase and the inertia  $M_{dva}$  will suddenly decrease, and the robot will immediately reduce the inertial behavior and reduce the displacement overshoot. Enlarge the figure to show that the proposed method ( $\alpha = 1.9$ ) reaches the peak 0.64 s earlier than the traditional method. During the robot retraction,  $K_{dva}$  is still larger and  $M_{dva}$  is still smaller



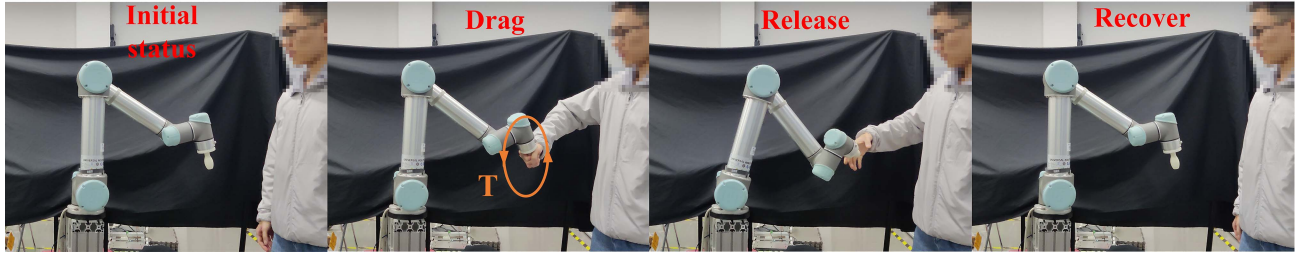


Fig. 8. Cartesian space orientation admittance control.

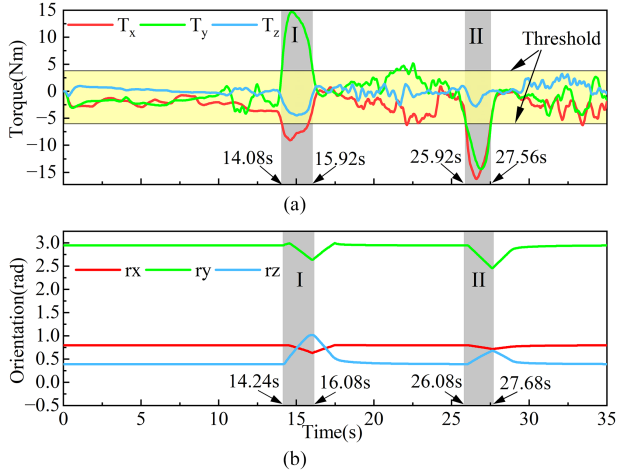


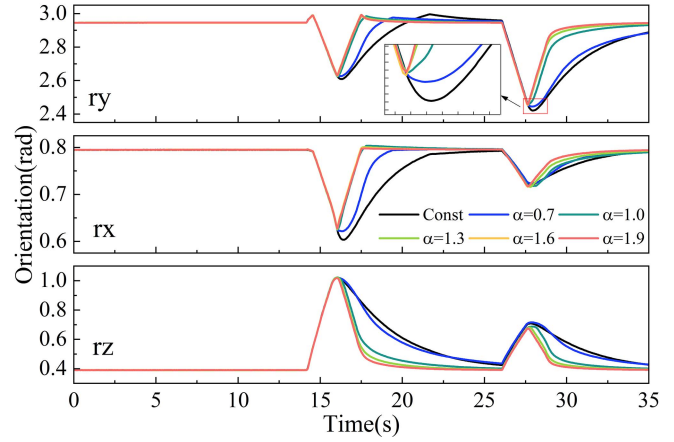
Fig. 9. Cartesian space orientation admittance control experiment. (a) Torque estimate of a virtual six-dimensional torque sensor. (b) Orientation of the flange center in base frame. Icons have the same meaning as in Fig. 6.

compared to traditional control. As the robot gradually returns to the initial position, the velocity gradually converges to 0, and the stiffness and inertia will return to the initial set values. An increase in  $\alpha$  is effective in reducing the robot motion time, but from  $\alpha = 1.6$  onwards, the increase in  $\alpha$  provides a limited improvement in time reduction.

**2) Cartesian Spatial Orientation Admittance Control:** The procedure of this experiment is similar to the Cartesian spatial position admittance control experiment, as shown in Fig. 8. It is just that the previous force is replaced with a torque, and the robot end only changes orientation.

As shown in Fig. 9, during force application phases, the virtual F/T sensor exhibited a 0.16 s latency from torque detection (14.08 s) to orientation adjustment (14.24 s) in Phase I, and an equivalent 0.16 s delay from detection (25.92 s) to positional response (26.08 s) in Phase II. For torque withdrawal scenarios, the system showed 0.16 s (15.92 s  $\rightarrow$  16.08 s) and 0.12 s (27.56 s  $\rightarrow$  27.68 s) recovery latencies in respective phases. The maximum observed latency between torque detection and robotic response remained below 0.2 s.

Fig. 10 shows that the proposed method ( $\alpha = 1.9$ ) reaches the peak value 0.32 s earlier than the traditional method, and the conclusions that can be drawn from the changed figure are the same as those in Fig. 7.

Fig. 10. Comparative Experiment of Cartesian space orientation admittance.  $M_d$ ,  $B_d$ , and  $K_d$  were the same as in previous experiments. The forces for this series of experiments were those recorded in Fig. 9 and not applied by the experimenter.TABLE IV  
PARAMETERS OF ADMITTANCE CONTROL FOR FRANKA

Coordinates	$M_d$	$B_d$	$K_d$	$\alpha$	$F_{tsd}$	$\dot{X}_{tsd}$
x	40	120	12	6	4 N	0.9 m/s
y	40	120	12	6	4 N	0.9 m/s
z	40	120	12	6	15 N	0.9 m/s
rx	4	6	2	3	2 Nm	—
ry	4	6	2	3	2 Nm	—
rz	4	6	2	3	2 Nm	—

#### D. Variable Parameter Admittance Control Based on Virtual F/T Sensor for Franka Emika Panda Robot

To demonstrate the universality of the proposed algorithm, we conducted experiments using a 7-DoF Franka Emika Panda robot, with parameter identification still referring to [10]. The experiment was conducted via the Franka control interface (FCI) using the libfranka interface. The Franka is equipped with torque sensors at link side to measure the drive torque directly. The FCI provides API for measuring the external force and serves as a reference for the virtual F/T sensor. Experiments have shown that the Franka virtual F/T sensor takes approximately 2.2 ms to perform calculations. The control cycle is set to 2.5 ms, which is greater than the sampling cycle of 1 ms (1000 Hz). So, establish two threads for data sampling and control to ensure smooth

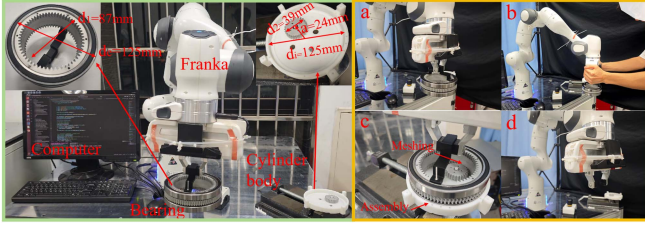


Fig. 11. Experimental equipment for Franka and bearing assembly process.

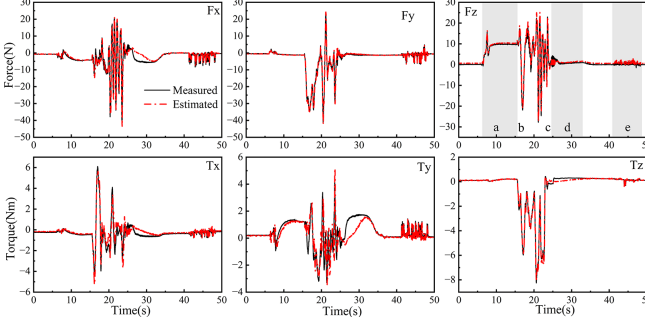


Fig. 12. Real sensor versus virtual sensor for Franka. e indicates that Franka is subject to unexpected external forces.

communication. Parameter settings are as shown in Table IV and in the following.

- 1) FKO:  $R = \text{diag}(0.08, 0.08, 0.08, 0.08, 0.01, 0.01, 0.01)$   
 $Q_p = \text{diag}(0.05, 0.05, 0.05, 0.05, 0.02, 0.02, 0.02)$   
 $Q_\tau = \text{diag}(1, 1, 1, 1, 1, 1, 1) \times 10^5$ .

We applied the proposed method to the complex assembly task of a bearing with an inner ring gear shown on the left side of Fig. 11. Franka moved the bearing ( $G = 9.2$  N) and assembled it with the cylinder fixed on the workbench under the guidance. This assembly involved two tasks: 1) Peg-in-hole assembly: The outer ring of the bearing is matched with the inner ring of the cylinder body. 2) Gear meshing: The inner ring of the bearing gear meshes with the gear inside the cylinder body. The experimental process is as follows: a) Franka grips the bearing. b) The Franka robot moves from the initial position to near the cylinder under the operator's guidance. c) The bearing is assembled with the cylinder with Franka's assistance, and the grippers are released. d) Franka returns to the initial position to prepare for the next assembly task, as shown on the right side of Fig. 11.

Fig. 12 shows the external force estimated by the virtual F/T sensor and the external force measured by libfranka. When Franka is unloaded, the zero drift of the virtual F/T sensor is  $(-0.43166, -0.53348, 0.83768, -0.16294, 0.13407, 0.09103)$ , which is significantly smaller than the zero drift of the UR5. The primary reason for this is that the torque sensor of the Franka is mounted on the link side, bypassing the reducer, resulting in a significant reduction in static friction. After hanging the bearing on the Franka, the estimated value for the  $z$ -axis stabilizes around 10.5 N, and after subtracting the zero drift, it is 9.66 N, which is close to the weight of the bearing. After

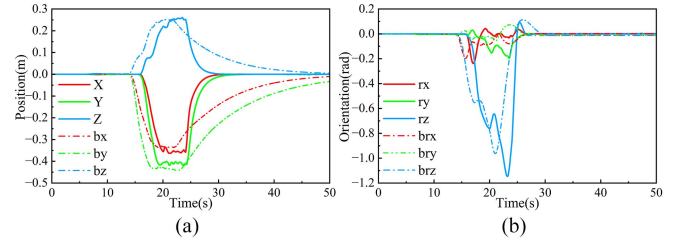


Fig. 13. Position (a) and orientation (b) during assembly. The dotted line indicates the position and orientation changes of traditional admittance control.

the experimenter dragged Franka for assembly experiments, the trend of changes in the virtual F/T sensor and measured values was basically the same, demonstrating the accuracy of the proposed virtual F/T sensor.

Fig. 13 shows the changes in Franka's position and orientation during the assembly process. Compared with traditional admittance control, the proposed variable parameter admittance control enables the robot to quickly return to its initial position after completing the assembly task. Combining Figs. 12 and 13, it can be seen that when the robot is subjected to external disturbances (not human forward movement), the robot maintains good stability and does not move.

During assembly, the pulling process requires the robot to be soft, while the recovery process requires the robot to be highly rigid. These two requirements are contradictory, but the proposed method effectively balances the two stages, thereby improving success rates and efficiency.

## V. CONCLUSION

This paper derives the robot dynamics model, FDO, GMO, and KFO, and verifies the feasibility of the three observers in joint torque detection. The KFO via FE discretization is selected as the virtual F/T sensor based on the estimation error, computation time, and parameter adjustment difficulty. The performance of real F/T sensor and virtual F/T sensor was compared on the 6-DoF UR5 and 7-DoF Franka robot. The experiment shows that the accuracy of virtual F/T sensor meets control requirements.

We propose a variable parameter Cartesian space admittance control algorithm based on virtual F/T sensor and apply it to the UR5 and Franka robot. Experiments on the UR robot show that the proposed algorithm enables the robot to respond quickly to external forces. Experiments on the Franka robot show that the proposed method can complete complex assembly tasks. Both experiments show that the proposed method can balance the parameter contradictions between the admittance control traction phase and the recovery phase to improve task success rate and efficiency.

The force threshold of the algorithm proposed can reach 4 and 20 N, which is much lower than the safety force threshold of 50 N specified in the ISO 10218-1 and ISO/TS 15066 standards. In addition, we have set speed threshold to ensure the safety of the experimenter, so the system complies with the above two standards.

In this article, the motor drive torque is obtained through the motor current and torque sensors at link side, without considering the significant effects of transmission friction, lag, vibration, and temperature [42]. Therefore, we will develop a more explicitly identified model of robot friction and dynamics, especially at low speed [43]. In addition, we will continue to study the application of virtual F/T sensor in the force control of large industrial robots (KUKA and FANUC) for more tasks, such as welding and gripping.

## REFERENCES

- [1] M. Javaid, A. Haleem, R. P. Singh, and R. Suman, "Substantial capabilities of robotics in enhancing industry 4.0 implementation," *Cogn. Robot.*, vol. 1, pp. 58–75, 2021.
- [2] C. Li, L. Zhu, G. Yang, and J. Zhang, "Zero-force drag and start-up torque compensation strategies for robots," *Robotica*, vol. 43, no. 3, pp. 926–944, 2025.
- [3] C. T. Landi, F. Ferraguti, C. Secchi, and C. Fantuzzi, "Tool compensation in walk-through programming for admittance-controlled robots," in *Proc. IECON 2016-42nd Annu. Conf. IEEE Ind. Electron. Soc.*, IEEE, 2016, pp. 5335–5340.
- [4] T. Xu, J. Fan, Q. Fang, J. Zhao, and Y. Zhu, "Robotic arm collision reaction strategies for safe human–robot interaction without torque sensors," *J. Mechan. Med. Biol.*, vol. 19, no. 07, 2019, Art. no. 1940034.
- [5] W. Deng, C. Zhang, Z. Zou, M. Gao, X. Wang, and W. Yu, "Peg-in-hole assembly of industrial robots based on object detection and admittance force control," in *Proc. 36th Youth Academic Annu. Conf. Chin. Assoc. Automat. (YAC)*, 2021, pp. 672–677.
- [6] S. Liu, L. Wang, and X. V. Wang, "Sensorless haptic control for human-robot collaborative assembly," *CIRP J. Manuf. Sci. Technol.*, vol. 32, pp. 132–144, 2021. [Online]. Available: <https://www.sciencedirect.com/science/article/pii/S1755581720301656>
- [7] P. Cao, Y. Gan, and X. Dai, "Model-based sensorless robot collision detection under model uncertainties with a fast dynamics identification," *Int. J. Adv. Robotic Syst.*, vol. 16, no. 3, May 2019, Art. no. 1729881419853713. [Online]. Available: <https://doi.org/10.1177/1729881419853713>
- [8] S. Mamedov and S. Mikhel, "Practical aspects of model-based collision detection," *Front. Robot. AI*, vol. 7, 2020, Art. no. 571574.
- [9] X. Yang, Z. Zhou, L. Li, and X. Zhang, "Collaborative robot dynamics with physical human–robot interaction and parameter identification with pinn," *Mechanism Mach. Theory*, vol. 189, 2023, Art. no. 105439.
- [10] Y. Huang, J. Ke, X. Zhang, and J. Ota, "Dynamic parameter identification of serial robots using a hybrid approach," *IEEE Trans. Robot.*, vol. 39, no. 2, pp. 1607–1621, Apr. 2023.
- [11] W.-H. Chen, "Disturbance observer based control for nonlinear systems," *IEEE/ASME Trans. Mechatron.*, vol. 9, no. 4, pp. 706–710, Dec. 2004.
- [12] S. Haddadin, A. De Luca, and A. Albu-Schäffer, "Robot collisions: A survey on detection, isolation, and identification," *IEEE Trans. Robot.*, vol. 33, no. 6, pp. 1292–1312, Dec. 2017.
- [13] H. Xing, L. Ding, K. Xia, J. Chen, H. Gao, and Z. Deng, "Sensorless end-effector force estimation of multi-DOF manipulators using semiparametric joint model and generalized momentum observer," *IEEE Sensors J.*, vol. 25, no. 13, pp. 23720–23731, Jul. 2025.
- [14] C.-n. Ho and J.-B. Song, "Collision detection algorithm robust to model uncertainty," *Int. J. Control, Automat. Syst.*, vol. 11, no. 4, pp. 776–781, 2013.
- [15] S.-D. Lee, K.-H. Ahn, and J.-B. Song, "Subspace projection-based collision detection for physical interaction tasks of collaborative robots," *Int. J. Precis. Eng. Manuf.*, vol. 20, pp. 1119–1126, 2019.
- [16] S. Long, X. Dang, and J. Huang, "Fooso-net: A specific neural network for fast sensorless robot manipulator torque estimation," *Neural Netw.*, vol. 168, pp. 14–31, 2023.
- [17] Y. Wei, J. Wang, W. Li, X. Du, X. Yu, and L. Guo, "Composite disturbance filtering for interaction force estimation with online environmental stiffness exploration," *IEEE/ASME Trans. Mechatron.*, vol. 30, no. 3, pp. 1983–1993, Jun. 2024.
- [18] M. Li, R. Kang, D. T. Branson, and J. S. Dai, "Model-free control for continuum robots based on an adaptive Kalman filter," *IEEE/ASME Trans. Mechatron.*, vol. 23, no. 1, pp. 286–297, Feb. 2017.
- [19] S. Li, D. Shi, Y. Lou, W. Zou, and L. Shi, "Generalized multikernel maximum correntropy Kalman filter for disturbance estimation," *IEEE Trans. Autom. Control*, vol. 69, no. 6, pp. 3732–3747, Jun. 2023.
- [20] J. Hu and R. Xiong, "Contact force estimation for robot manipulator using semiparametric model and disturbance kalman filter," *IEEE Trans. Ind. Electron.*, vol. 65, no. 4, pp. 3365–3375, Apr. 2017.
- [21] T. T. Phuong et al., "Disturbance observer and kalman filter based motion control realization," *IEEJ J. Ind. Appl.*, vol. 7, no. 1, pp. 1–14, 2018.
- [22] T. Sun, J. Sun, B. Lian, and Q. Li, "Sensorless admittance control of 6-dof parallel robot in human-robot collaborative assembly," *Robot. Comput.-Integr. Manuf.*, vol. 88, 2024, Art. no. 102742. [Online]. Available: <https://www.sciencedirect.com/science/article/pii/S0736584524000280>
- [23] D. Reyes-Uquillas and T. Hsiao, "Safe and Intuitive Manual Guidance of a Robot Manipulator Using Adaptive Admittance Control Towards Robot Agility," *Robotics and Computer-Integrated Manufacturing*, vol. 70, 2021, Art. no. 102127.
- [24] A.-N. Sharkawy and P. N. Koustoumpardis, "Human–robot interaction: A review and analysis on variable admittance control, safety, and perspectives," *Machines*, vol. 10, no. 7, 2022. [Online]. Available: <https://www.mdpi.com/2075-1702/10/7/591>
- [25] Y. Aydin, D. Sirintuna, and C. Basdogan, "Towards collaborative drilling with a cobot using admittance controller," *Trans. Inst. Meas. Control*, vol. 43, no. 8, pp. 1760–1773, 2021.
- [26] Y. M. Hamad, Y. Aydin, and C. Basdogan, "Adaptive human force scaling via admittance control for physical human-robot interaction," *IEEE Trans. Haptics*, vol. 14, no. 4, pp. 750–761, Oct./Dec. 2021.
- [27] C. Wang and J. Zhao, "Based on human-like variable admittance control for human–robot collaborative motion," *Robotica*, vol. 41, no. 7, pp. 2155–2176, 2023.
- [28] J. Cho, D. Choi, and J. H. Park, "Sensorless variable admittance control for human–robot interaction of a dual-arm social robot," *IEEE Access*, vol. 11, pp. 69366–69377, 2023.
- [29] G. Peng, C. P. Chen, and C. Yang, "Neural networks enhanced optimal admittance control of robot–environment interaction using reinforcement learning," *IEEE Trans. Neural Netw. Learn. Syst.*, vol. 33, no. 9, pp. 4551–4561, Sep. 2021.
- [30] C. Passenberg, A. Peer, and M. Buss, "A survey of environment-, operator-, and task-adapted controllers for teleoperation systems," *Mechatronics*, vol. 20, no. 7, pp. 787–801, 2010.
- [31] L. J. Love and W. J. Book, "Force reflecting teleoperation with adaptive impedance control," *IEEE Trans. Systems, Man, Cybernetics, Part B (Cybernetics)*, vol. 34, no. 1, pp. 159–165, Feb. 2004.
- [32] J. J. Abbott, P. Marayong, and A. M. Okamura, "Haptic virtual fixtures for robot-assisted manipulation," in *Proc. Robot. Research: Results 12th Int. Symp.*, Springer, 2007, pp. 49–64.
- [33] G. Kang, H. S. Oh, J. K. Seo, U. Kim, and H. R. Choi, "Variable admittance control of robot manipulators based on human intention," *IEEE/ASME Trans. Mechatron.*, vol. 24, no. 3, pp. 1023–1032, Jun. 2019.
- [34] M. W. Spong, S. Hutchinson, and M. Vidyasagar, *Robot Modeling and Control*. John Wiley & Sons, Inc., 2020, doi: [10.1109/MCS.2021.3122271](https://doi.org/10.1109/MCS.2021.3122271).
- [35] M. Van Damme et al., "Estimating robot end-effector force from noisy actuator torque measurements," in *Proc. IEEE Int. Conf. Robot. Autom. IEEE*, 2011, pp. 1108–1113.
- [36] A. De Luca and R. Mattone, "Actuator failure detection and isolation using generalized momenta," in *Proc. IEEE Int. Conf. Robot. Automat.*, vol. 1, IEEE, 2003, pp. 634–639.
- [37] A. Wahrburg, J. Börs, K. D. Listmann, F. Dai, B. Matthias, and H. Ding, "Motor-current-based estimation of cartesian contact forces and torques for robotic manipulators and its application to force control," *IEEE Trans. Automat. Sci. Eng.*, vol. 15, no. 2, pp. 879–886, Apr. 2018.
- [38] F. Cao, P. D. Docherty, S. Ni, and X. Chen, "Contact force and torque sensing for serial manipulator based on an adaptive Kalman filter with variable time period," *Robot. Comput.-Integr. Manuf.*, vol. 72, 2021, Art. no. 102210.
- [39] D. Zurlo, T. Heitmann, M. Morlock, and A. De Luca, "Collision detection and contact point estimation using virtual joint torque sensing applied to a cobot," in *Proc. IEEE Int. Conf. Robot. Automat.*, 2023, pp. 7533–7539.
- [40] C. Van Loan, "Computing integrals involving the matrix exponential," *IEEE Trans. Autom. Control*, vol. 23, no. 3, pp. 395–404, Jun. 1978.
- [41] Z. Zhang, Y. Chen, D. Zhang, and Q. Tong, "Research on numerical compensation method of tandem force sensor installed at the end of industrial robot," in *Proc. 5th Int. Conf. Automat. Control Robot Eng.*, 2020, pp. 725–731.
- [42] E. Villagrossi et al., "A virtual force sensor for interaction tasks with conventional industrial robots," *Mechatronics*, vol. 50, pp. 78–86, 2018.
- [43] M. Capurso, M. M. G. Ardakani, R. Johansson, A. Robertsson, and P. Rocco, "Sensorless kinesthetic teaching of robotic manipulators assisted by observer-based force control," in *Proc. IEEE Int. Conf. Robot. Automat.*, 2017, pp. 945–950.





**Yanjiang Huang** (Member, IEEE) received the Ph.D. degree in precision mechanical engineering from the University of Tokyo, Tokyo, Japan, in 2013.

From September 2020, he became a Professor with the South China University of Technology, Guangzhou, China. His main research interests are robotic manipulation, human–robot interaction, and robot system design.



**Xianmin Zhang** (Member, IEEE) received the Ph.D. degree in mechanical engineering from the Beijing University of Aeronautics and Astronautics, Beijing, China, in 1993.

He is the Professor with the School of Mechanical and Automotive Engineering, South China University of Technology, Guangzhou, China, from 2003. His research interests include robotics and precision instrument analysis and design.



**Xinyu Liu** received the B.S. degree in mechanical design, manufacturing, and automation from the Xiangtan University, Xiangtan, China, in 2023. He is currently working toward the master's degree in mechanical engineering with the School of Mechanical and Automotive Engineering, South China University of Technology, Guangzhou, China.

His current research interests include admittance control and human–robot interaction.



**Lixin Yang** received the Ph.D. degree in mechanical engineering from the South China University of Technology, Guangzhou, China, in 2018.

She is an Associate Professor with the School of Mechanical and Automotive Engineering, South China University of Technology, Guangzhou, China, from 2019. Her research interests include robotics, mechanism dynamics, and control.



**Jianhong Ke** received the master's degree in mechanical engineering from the School of Mechanical and Automotive Engineering, South China University of Technology, Guangzhou, China, in 2023.

His current research interests include robot dynamic modeling and adaptive control.



**Jun Ota** (Member, IEEE) received the Ph.D. degree in precision mechanical engineering from the University of Tokyo, Tokyo, Japan, in 1991.

From 2009, he was a Professor with Research into Artifacts, Center for Engineering (RACE), University of Tokyo. His research interests include multiagent robot systems and design support for large-scale production handling systems.